GDCh

Research Article

Angewandte
Chemie
International Edition
www.angewandte.org

Solar Cells

Asymmetrified Benzothiadiazole-Based Solid Additives Enable All-Polymer Solar Cells with Efficiency Over 19 %

Tianqi Chen, Yanyi Zhong, Tainan Duan,* Xian Tang, Wenkai Zhao, Jiaying Wang, Guanghao Lu, Guankui Long, Jiangbin Zhang,* Kai Han, Xiangjian Wan, Bin Kan,* and Yongsheng Chen

Abstract: Disordered polymer chain entanglements within all-polymer blends limit the formation of optimal donor-acceptor phase separation. Therefore, developing effective methods to regulate morphology evolution is crucial for achieving optimal morphological features in all-polymer organic solar cells (APSCs). In this study, two isomers, 4,5-difluorobenzo-*c*-1,2,5-thiadiazole (SF-1) and 5,6-difluorobenzo-*c*-1,2,5-thiadiazole (SF-2), were designed as solid additives based on the widely-used electron-deficient benzothiadiazole unit in nonfullerene acceptors. The incorporation of SF-1 or SF-2 into PM6:PY-DT blend induces stronger molecular packing via molecular interaction, leading to the formation of continuous interpenetrated networks with suitable phase-separation and vertical distribution. Furthermore, after treatment with SF-1 and SF-2, the exciton diffusion lengths for PY-DT films are extended to over 40 nm, favoring exciton diffusion and charge transport. The asymmetrical SF-2, characterized by an enhanced dipole moment, increases the power conversion efficiency (PCE) of PM6:PY-DT-based device to 18.83 % due to stronger electrostatic interactions. Moreover, a ternary device strategy boosts the PCE of SF-2-treated APSC to over 19 %. This work not only demonstrates one of the best performances of APSCs but also offers an effective approach to manipulate the morphology of all-polymer blends using rational-designed solid additives.

Introduction

All-polymer solar cells (APSCs), comprised of polymer donors and polymer acceptors, demonstrate mechanical robustness and enhanced device stability, making them promising for flexible and stretchable devices.[1] The power conversion efficiency (PCE) of APSCs has surpassed 18 % due to advancements in polymer photovoltaic materials,[2] particularly polymerized small molecule acceptors, and device fabrication techniques.[1a,3] However, APSCs still exhibit lower PCE compared to solar cells utilizing polymeric donors and small-molecule acceptors. The inferior performance of APSCs primarily stems from challenges in controlling morphology, influenced by the extensive chain entanglement resulting from large polymer molecular size.[4] Consequently, unfavorable phase separation and disordered molecular packing often occur during film formation. Achieving a well-defined phase-separated morphology with appropriate domain size, crucial for efficient exciton separation, charge carrier transport, and recombination, is essential for high-efficiency APSCs.[5]

Various strategies, such as post-treatment (e.g., solvent vapor annealing, thermal annealing), introduction of a third component, and incorporation of additives, have been employed to optimize the morphology of all-polymer blends.[1h,6] Among these methods, the addition of additives to modulate the interactions of photovoltaic materials stands out as an efficient and straightforward approach, and is now widely utilized. Traditional solvent additives, like 1,8-

[*] T. Chen, W. Zhao, J. Wang, G. Long, B. Kan
School of Materials Science and Engineering, National Institute for Advanced Materials, Nankai University, 300350 Tianjin, China
E-mail: kanbin04@nankai.edu.cn

T. Chen, X. Wan, Y. Chen
State Key Laboratory and Institute of Elemento-Organic Chemistry, Frontiers Science Center for New Organic Matter, The Centre of Nanoscale Science and Technology and Key Laboratory of Functional Polymer Materials, Renewable Energy Conversion and Storage Center (RECAST), College of Chemistry, Nankai University, 300071 Tianjin, China

Y. Zhong, J. Zhang, K. Han
College of Advanced Interdisciplinary Studies, National University of Defense Technology, 410073 Changsha, China
E-mail: zhangjiangbin@nudt.edu.cn

T. Duan
Chongqing Institute of Green and Intelligent Technology, Chongqing School, University of Chinese Academy of Sciences (UCAS Chongqing), Chinese Academy of Sciences, 400714 Chongqing, China
E-mail: tnduan@cigit.ac.cn

X. Tang, G. Lu
Institute of Science and Technology, Xi'an Jiaotong University, 710054 Xi'an, China

J. Zhang, K. Han
Nanhu Laser Laboratory, National University of Defense Technology, 410073 Changsha, China

J. Zhang
Hunan Provincial Key Laboratory of High Energy Laser Technology, National University of Defense Technology, 410073 Changsha, China

diiodooctane[7] and 1-chloronaphthalene,[8] are commonly used to enhance photovoltaic performance by facilitating film formation. However, solvent additives typically have a high boiling point, necessitating elevated heating temperatures and leaving behind residual additives, which is detrimental to device long-term stability.[9] In response, solid additives have emerged as an alternative to solvent additives for enhancing device efficiency.[3e] Solid additives often share structural segments with active layer materials, promoting tight π–π stacking and exhibiting a wide concentration range tolerance, thereby improving device reproducibility and stability.[10] Yan et al. proposed 2-chloronaphthalene as a solid additive to replace 1-chloronaphthalene, achieving high device performance.[11] Chen et al. introduced a broad-spectrum volatile solid additive, 2,5-dichlorothieno-[3,2-b]thiophene, to fabricate a PM6:Y6 binary device with optimized fibril networks and phase distributions, resulting in a PCE of 18.20%.[12]

To the best of our knowledge, there are quite few reports about solid additives that have been successfully applied for regulating the morphology of polymer active layers. As a typical example, Sun et al. fabricated an APSC based on PM6:PY-DT with a PCE of over 17% by adopting 2-methoxynaphthalene (2-MN), effectively manipulating the molecular aggregation and resulting in a favorable phase-separated morphology.[13] We obtained a PCE of over 18% based on PM6:PY-IT using the perhalogenated thiophene SA-T1 as a solid additive.[14] Liu et al. employed 1,4-diiodobenzene (DIB) to control the morphology of PM6:PY-IT blends and achieved a PCE over 19% when coupled with thermal annealing and solvent vapor annealing.[1a] So far, most reported solid additives are based on electron-rich units such as thiophene and benzene, but electron-deficient unit-based small molecules with structural segments similar to those of active components also theoretically assist in regulating the morphology of the films by serving as additives through interactions with active layer materials.[15] As a classic electron-deficient unit, benzothiadiazole plays an indispensable and omnipotent role in developing organic optoelectronic materials.[16] In recent years, Y-series electron acceptors based on the benzothiadiazole core have achieved unprecedented success in organic photovoltaics.[17] The various intermolecular stacking pattern induced by benzothiadiazole is one of the fundamental reasons for the outstanding performance of Y-series acceptors.[18] Therefore, it is reasonable to believe that through delicate molecular design, solid additives based on benzothiadiazole can play a positive role in enhancing the performance of organic photovoltaic devices.

In this work, we designed and synthesized two solid additives with positional isomerization based on the benzothiadiazole units, which are widely used in photovoltaic materials, namely, SF-1 (4,5-difluorobenzo-*c*-1,2,5-thiadiazole) and SF-2 (5,6-difluorobenzo-*c*-1,2,5-thiadiazole), to regulate the morphology of PM6:PY-DT blend. Detailed morphological characterization revealed that two solid additives, SF-1 and SF-2, can effectively control the morphology of the BHJ through "chain-breaking"-like and "self-healing"-like processes. Besides, the ideal vertical

phase distribution with an acceptor-rich phase near the cathode and a donor-rich phase near the anode was incorporated with the formation of bi-continuous interpenetrating networks, and the device parameters fill factor (*FF*) and short-circuit current (J_{sc}) were effectively elevated. Moreover, the exciton diffusion length (L_D) increased from 38.04 nm for the additive-free film to 41.01 nm for the SF-1-film and 41.48 nm for the SF-2-film, supporting more efficient charge-transfer process. The asymmetrically featured SF-2 shows an enhanced dipole moment, leading to stronger interactions with active materials than those of SF-1, which promotes the generation of the most suitable donor/acceptor (D/A) phase separation in the active layer and contributes to faster charge mobility and extraction. Therefore, a high PCE of 18.83% was obtained for the PM6:PY-DT-based binary device with SF-2 as an additive, which is higher than that obtained for the device processed with SF-1 (17.83%). Moreover, a satisfactory PCE of 19.02% was obtained for the SF-2-treated ternary device PM6:PY-DT:L8-BO. Our results offer valuable methods for obtaining favorable all-polymer blend morphologies and insights into designing high-performance solid additives.

Results and Discussion

The chemical structures of the photoactive materials, SF-1 and SF-2 are displayed in Figure 1a. The synthetic routes of additives are illustrated in the Supporting Information (Scheme S1), which can be facilely obtained through a one-step reaction in high yield. The introduction of fluorine can effectively enhance the π–π interactions between the additives and the donor/acceptor molecules, while not significantly reducing the volatility of the additives. This ensures that the additives can be completely removed under mild temperature during the post-treatment. By adjusting the positions of the two fluorine atoms, two isomeric additives were obtained. To conduct a preliminarily investigation of them, the single crystals of SF-2 was cultivated and compared with SF-1. The single crystals of SF-2 were obtained by the slow evaporation of its saturated chloroform solution (CCDC No. 2364666, Figure S1 and Table S1). As can be seen in Figure 1b, the SF-1 with symmetric structure is packed in a triclinic unit cell of the P$\bar{1}$ space group in single crystal. It exhibits a double-orientation stacking pattern in the single crystal, with a relatively short π–π stacking distance between molecules (3.36 Å). The SF-2 molecule with asymmetric structure is packed in a monoclinic unit cell of the P2₁/c space group in single crystal. Distinct from SF-1, SF-2 exhibits a four-orientation stacking pattern in the single crystal, with a larger intermolecular stacking distance (3.43 Å) and weaker interactions between adjacent molecules. From the single crystal structures, it can be inferred that, compared to SF-1, the asymmetric SF-2 is not only easier to remove from the donor-acceptor blend film but also has the potential to induce the formation of a more interpenetrating network structure with multiple stacking modes in the blend film.
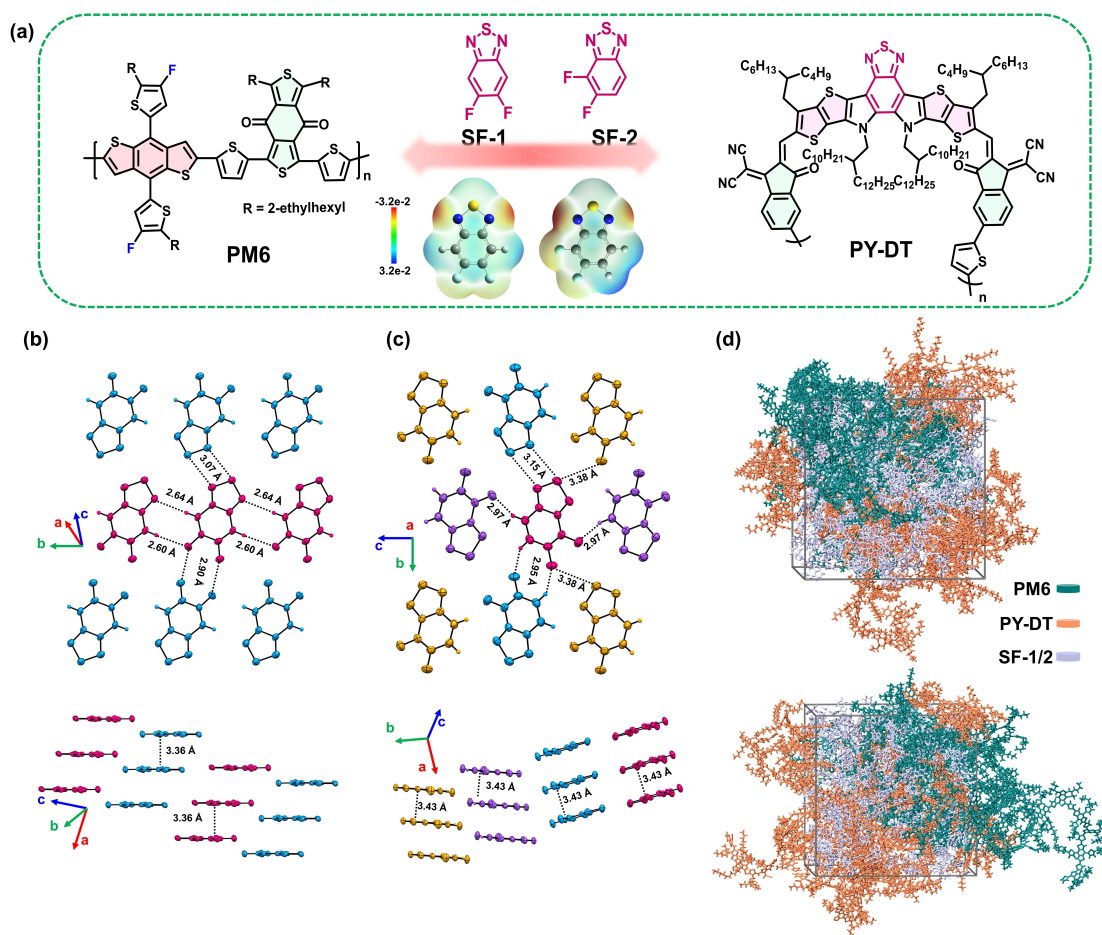
Figure 1. (a Chemical structures of PM6, PY-DT, SF-1 and SF-2 along with their ESP distributions, respectively. (b–c) Single-crystal packing diagram of SF-1 and SF-2, respectively. (d) MD simulation of the blend film evolution process treated with SF-1 or SF-2.

The electrostatic potential (ESP) surfaces of SF-1 and SF-2 were calculated by density functional theory (DFT). As shown in Figure 1a, the ESP surfaces of SF-1 and SF-2 present a positive distribution, indicating their electron deficiency, which facilitates interactions with the electron-rich units in the active materials. We determined that 100 % of the weight loss of the two additives occurred before 100 °C through thermogravimetric analysis (TGA) of the samples heated from 25 to 300 °C at a scan rate of 10 K/min (Figure S2a). We further investigated the thermal properties of the two solid additives through differential scanning calorimetry (DSC) measurements. As displayed in Figure S2b, SF-1 and SF-2 exhibited low melting points of 67.5 and 56.8 °C, respectively, indicating their high volatility.

The high volatility ensures that the two solid additives can be removed completely from the active layer without any residual after thermal annealing. In addition, we traced the solid additives in the blended films by Fourier transform infrared (FT-IR) spectroscopy, as shown in Figure S3. Significant differences were observed in the FT-IR spectra between the blend films with and without additives. The FT-IR spectrum exhibited the characteristic peaks of SF-1 at 858 and 620 cm^{-1} in the film treated with SF-1 before thermal annealing, but the signal of SF-1 did not appear in

the spectrum of the as-cast film. The nearly identical FT-IR spectra of the as-cast film and the SF-1-processed film after thermal annealing revealed that the additive SF-1 could be completely removed after applying the post-treatment of thermal annealing. The characteristic FT-IR peaks at 872 and 616 cm^{-1} for the additive SF-2 are similar to those for SF-1 due to its isomeric structure, and the same phenomenon was also observed for the as-cast film, the SF-2-treated film, and the film simultaneously treated with SF-2 and thermal annealing. By observing the FT-IR signals of SF-1 or SF-2, it could be inferred that SF-1 or SF-2 was present in the PM6:PY-DT blend film under spin-coating conditions and was completely removed after thermal annealing treatment. The ultraviolet–visible (UV–Vis) absorption spectra of the blended films cast with different additives are plotted in Figure S4. Compared with the as-cast film, the SF-1- or SF-2-processed films in combination with thermal annealing exhibited broader absorption ranges of PM6 and PY-DT, indicating that the molecular packing of the active materials was influenced by the introduction of SF-1 or SF-2, which maximized light utilization.

To explore the interaction between additives and active components and understand their working mechanism, a molecular dynamics (MD) approach (for detailed descrip-

tions, refer to the Supporting Information) was utilized to simulate the film evolution process with additives, as depicted in Figure 1d. Further energy analysis was performed to explore the effects of SF-1/SF-2 on the donor and acceptor, and detailed data are summarized in Table S2. We found that van der Waals forces were the main interactions between the SF-1/SF-2 additive and the active components. In addition, the two additives interact not only with the polymer donor but also with the acceptor, and it seems that there is no preference for interactions with the donor or the acceptor. Notably, compared with SF-1, SF-2 exhibited stronger van der Waals and electrostatic interactions with both PM6 and PY-DT. Interestingly, an apparent increase in electrostatic interactions was noted when SF-2 was employed as an additive. This is attributed to the larger dipole moment of SF-2 (2.05 D) compared to SF-1 (0.19 D) due to the presence of unsymmetrical fluorine atoms (refer to Figure S5). The film evolution process for the PM6:PY-DT blend after the removal of SF-1/SF-2 was simulated and shown in Figure S6. PM6 was divided into two segments, labeled as C and E, while PY-DT was divided into four segments, labeled as F, A, D, and A′ (Figure S7). In total, eight different packaging conditions were established. To obtain detailed analyses of the amorphous forms studied in the present work, we analyzed the number of dimer packing (defined the formation of a dimer as occurring when the atomic distance between two adjacent dimers is less than 5 Å) arising from these eight different packing conditions. As shown in Table S3, the PM6:PY-DT blend with SF-2 exhibits a total stacking count of 27.98 per unit volume after the removal of SF-2. In contrast, the PM6:PY-DT blend with the addition of SF-1 shows a total stacking count of 23.02. The higher stacking count of the PM6:PY-DT blend after the removal of SF-2 and the stronger interactions between SF-2 and active materials may promote the formation of a suitable phase separation, enhancing the J_{sc} and FF of the devices.

To unveil the influence of two isomeric additives on the degree of molecular ordering of the donor and acceptor, the morphology of the pristine films was analyzed through grazing incidence wide-angle X-ray scattering (GIWAXS) measurements. Two-dimensional GIWAXS diffraction patterns of the pristine films processed with and without SF-1/2 additives for PM6 and PY-DT, along with corresponding line-cut profile curves in the out-of-plane (OOP) and in-

plane (IP) directions, are depicted in Figure S8. The results in Table S4 demonstrated that the addition of SF-1 and SF-2 could enhance the PM6 molecular packing. Similar but mild trends were observed for the pure PY-DT films. The above discussions suggested that the addition of SF-1 and SF-2 was favorable for building structures with stronger π–π stacking and longer CLs but did not change the preferential face-on orientation, facilitating charge transport.

To evaluate the photovoltaic performance of SF-1 and SF-2 as additives in APSCs, we fabricated devices with a conventional structure of ITO/HTL (hole transport layer)/BHJ/PNDIT-F3N/Ag, and PM6:PY-DT was used as the BHJ component. The fabrication procedures are outlined in the Supporting Information, and the optimized device parameters with different additive contents are summarized in Table S5. The current density–voltage (J–V) curves of the optimal APSCs based on PM6:PY-DT are depicted in Figure 2, with corresponding photovoltaic parameters summarized in Table 1. The initial as-cast device employing PM6:PY-DT exhibited a modest PCE of 15.17% due to the limited J_{sc} of 24.81 mA cm^{-2} and FF of 62.7%. However, the high V_{oc}, attributed to the low E_{loss} of 0.495 eV for PM6:PY-DT blend (Table S6, and Figure S9–S10), provided a favorable foundation for obtaining high-performance device. Upon the addition of SF-1 and SF-2 additives to the PM6:PY-DT blend, significant enhancements in J_{sc} and FF were achieved while maintaining a high V_{oc}, resulting in high PCEs of 17.83% for SF-1 and 18.83% for SF-2. This improvement is credited to the precise adjustment of the two additives on blend morphology and efficient exciton dynamics. In addition, the SF-2-treated PM6:PY-DT device obtained a superior J_{sc} of 25.99 mA cm^{-2} and FF of 74.5% compared to those of the SF-1-treated devices, which led to a high PCE of 18.83%, among the best PCE reported for binary APSCs (Figure 2c, and Table S7). The enlarged dipole moment of asymmetric SF-2, which induces more ordered molecules conducive to effective charge transport, supported the increased J_{sc} and FF, accounting for its high PCE. Moreover, we fabricated solar devices with active areas of 1 cm^2 by imposing the same preparation conditions as those used for the small-area SF-2-treated devices, and a PCE of ~16% was obtained. Furthermore, the SF-2-processed ternary device (PM6:PY-DT:L8-BO) achieved a PCE of more than 19%, and Figure S11 displays the corresponding J–V curve. To our knowledge, this excellent

Table 1: Photovoltaic parameters of OSCs based on PM6:PY-DT processed with different conditions.

Active layer	V_{oc} (V)	J_{sc} (mA cm^{-2})	$J_{sc, cal}$ (mA cm^{-2})	FF (%)	PCE (%)
PM6:PY-DT	0.972 (0.975 ± 0.002)	24.81 (24.55 ± 0.22)	23.75	62.7 (62.5 ± 0.7)	15.17 (15.02 ± 0.25)
PM6:PY-DT (SF-1)	0.964 (0.964 ± 0.002)	25.36 (25.13 ± 0.31)	24.42	72.5 (72.5 ± 0.7)	17.83 (17.63 ± 0.12)
PM6:PY-DT (SF-2)	0.970 (0.967 ± 0.002)	25.99 (25.77 ± 0.16)	24.84	74.5 (74.4 ± 0.3)	18.83 (18.58 ± 0.14)
PM6:PY-DT:L8-BO[a]	0.961 (0.959 ± 0.002)	26.50 (26.43 ± 0.10)	25.26	74.5 (74.4 ± 0.1)	19.02 (18.92 ± 0.11)

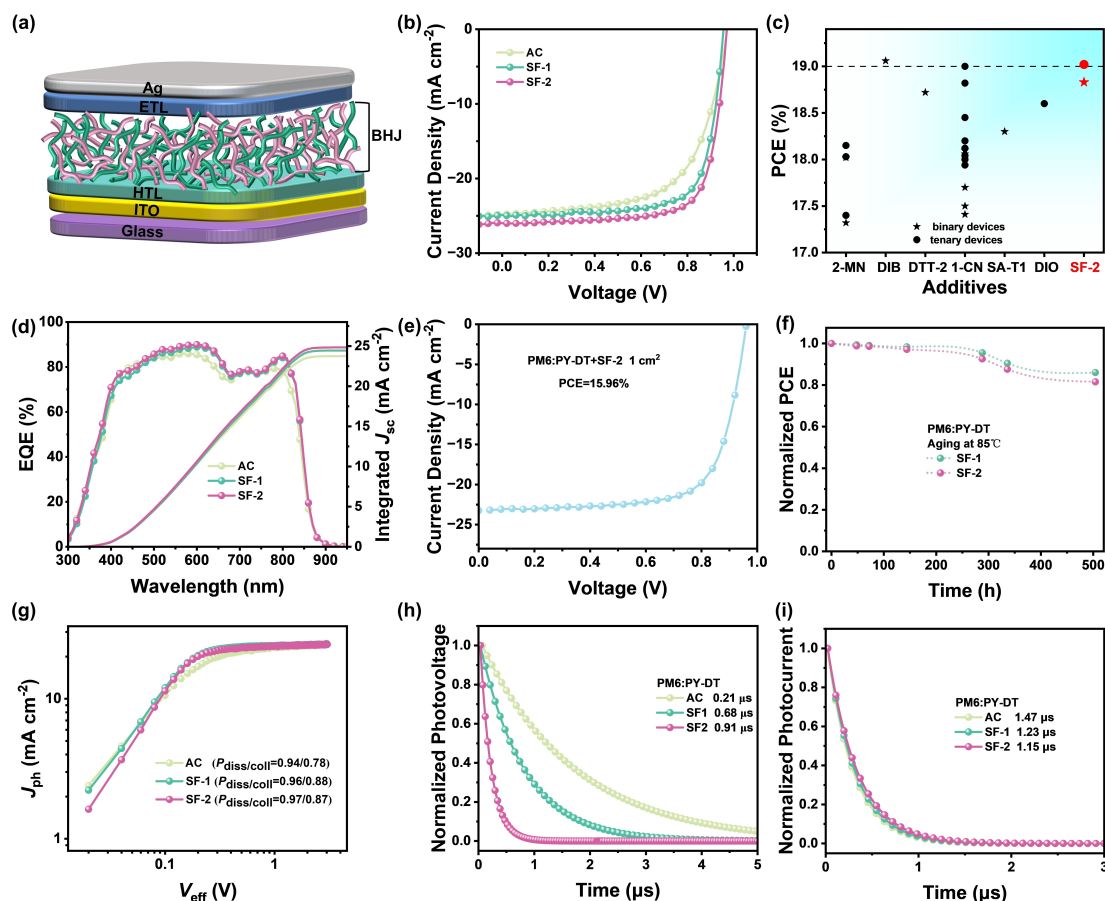[a] The device was processed with additive SF-2.

Figure 2. (a) Device structure used in this work. (b) *J–V* curves of PM6 : PY-DT-based devices processed with different conditions. (c) A summary of the PCE of efficient APSCs with different additives reported in the literature. (d) EQE curves and integrated *J*sc curves of PM6 : PT-D devices processed with different conditions. (e) *J–V* curves of large-area PM6 : PY-DT-based device (1 cm²) processed with SF-2. (f) Thermal stability of two optimal devices processed with SF-1 and SF-2. Plots of (g) *J*ph versus *V*eff, (h) TPV, and (i) TPC of the devices based on PM6 : PY-DT with different conditions.

result ranks in the best PCE obtained for ternary APSCs (Table S8), revealing the successful application of SF-2 in optimizing multicomponent devices.

The different J_{sc} values derived from the *J–V* curves were clarified through external quantum efficiency (EQE) measurements. The resultant integrated J_{sc} values of the as-cast, SF-1-, and SF-2-based devices are 23.75, 24.42, and 24.84 mA cm⁻², respectively, which are consistent with the increased J_{sc} observed from the *J–V* curves, as shown in Figure 2d. In detail, the $J_{sc,cal}$ values reached 15.00, 15.33, and 15.63 mA cm⁻² for the as-cast, SF-1-, and SF-2-based devices at 300–680 nm, respectively. In the 680–1000 nm region, the integrated $J_{sc,cal}$ values were 8.75, 9.09, and 9.21 mA cm⁻². These above results clarified that the additives have functions on both donor and acceptor, and the improvement of photoelectric response in the donor absorption region (300–680 nm) of the treated devices is slightly higher than the acceptor (680–1000 nm). In addition, the higher J_{sc} of the SF-2- device than of the SF-1 device was attributed to the enhanced EQE response, which corresponded with the conclusion that stronger interactions existed between SF-2 and the active materials. The optimal

binary devices with SF-1 or SF-2 retained ~80% of their PCEs after thermal aging for more than 500 h under continuous heating at 85 °C, indicating good thermal stability.

To elucidate the difference in device performance caused by J_{sc}, which is intimately related to charge recombination in devices, the *J–V* curves under various light intensities (P_{light}) were measured to probe the charge recombination loss. From the J_{sc} versus P_{light} curves, comparable α values of 0.99 were obtained for the as-cast and additive-treated devices, which indicates weak bimolecular recombination in the devices (Figure S12). We explore the exciton dissociation processes by measuring the relationship between the effective voltage (V_{eff}) and photocurrent density (J_{ph}). As shown in Figure 2g, exciton dissociation probability (P_{diss}) values of 0.94, 0.98, and 0.97 were attained for devices without, with SF-1 and with SF-2, respectively, and the corresponding exciton collection probability (P_{coll}) values were 0.78, 0.88, and 0.87, respectively. The devices processed with SF-1 and SF-2 exhibited more efficient exciton dissociation and collection processes, supporting the improved J_{sc} values. In addition, transient photovoltage (TPV) and

Angew. Chem. Int. Ed. **2024**, e202412983 (5 of 10)

© 2024 Wiley-VCH GmbH

transient photocurrent (TPC) measurements were carried out to evaluate the effects of the SF-1 and SF-2 additives on the carrier lifetime and charge extraction time (Figure 2h–i). The OSCs with SF-1 and SF-2 have carrier lifetimes of 0.68 and 0.91 μs, respectively, which are longer than that of the as-cast device (0.21 μs). The charge extraction times of the as-cast, SF-1-based, and SF-2-based devices are 1.15, 1.47, and 1.23 μs, respectively. These results suggested that the addition of the solid additives SF-1 or SF-2 could effectively suppress charge recombination and promote charge extraction in the devices, which could correspond to the improved J_{sc} and FF. The mobility of devices subjected to different treatments was studied by the space-charge limited current (SCLC) method. The hole mobility (μ_h) significantly improved to 1.30 and 1.61×10^{-3} cm^2 V^{-1} s^{-1} (compared to the μ_h of 0.83×10^{-3} cm^2 V^{-1} s^{-1} of the as-cast device) with the participation of SF-1 and SF-2, respectively, and there were no significant changes in the electron mobility (μ_e) (Figure S13 and Table S9). The increased charge transport with SF-1 and SF-2 as solid additives enabled PM6:PY-DT-based devices with enhanced J_{sc} and FF.

It is known that the vertical phase separation of BHJs, which consists of donors and acceptors, plays an important role in charge transfer and recombination, embodied in device parameters. Accurate morphology control of the active layer is essential for finely adjusting the phase distribution. We explored the effects of the solid additives SF-1 and SF-2 on the phase distribution and the vertical charge carrier dynamics by employing film depth-dependent light absorption spectroscopy (FLAS). The FLAS results of the PM6:PY-DT blend without and with additives are shown in Figure 3a–c, and the three blends exhibited relatively uniform absorption peaks for the donors and acceptors, which indicated that the energetic levels were uniformly distributed. The excitons in active layers need to dissociate into electrons and holes, which are actuated by built-in electric fields. We found that the excitons generated by the acceptor PY-DT approached the HTL, principally from the generation contours (Figure 3d–f), which implied that the interface of the HTL is pivotal to the efficiency of the devices.[19] The results of quantitative calculations of the distribution of donors and acceptors extracted from the FLAS spectra are displayed in Figure 3g–i. The composition distributions from top to bottom of the three blends under different conditions fluctuated similarly. There was acceptor-rich phase at the bottom near the cathode and a donor-
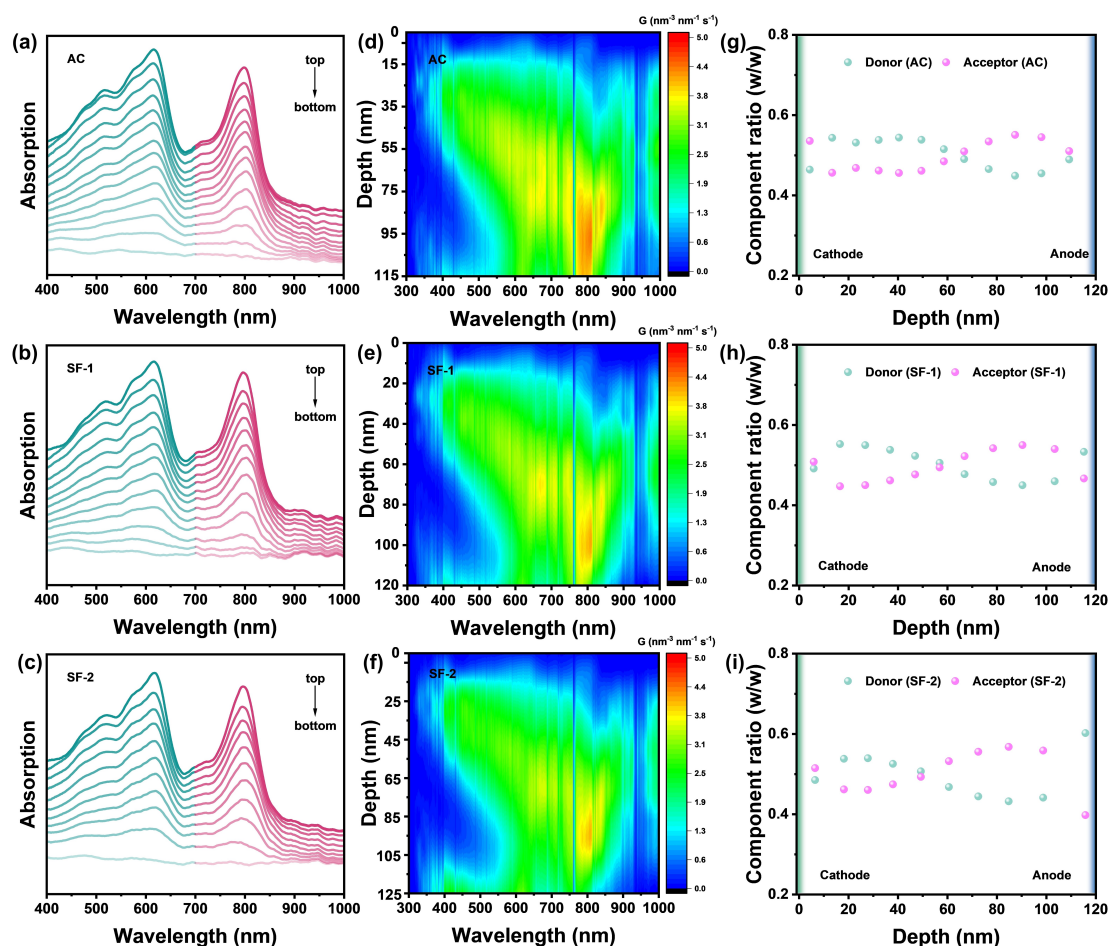

Figure 3. (a–c) The film-depth-dependent profiling light absorption spectra of as-cast, SF-1-treated and SF-2-treated PM6:PY-DT film, respectively. (d–f) Simulated exciton generation contours of as-cast, SF-1-treated and SF-2-treated PM6:PY-DT film, respectively. (g–i) The film-depth-dependent composition profiles extracted from the FLAS of as-cast, SF-1-treated and SF-2-treated PM6:PY-DT films, respectively.

Angew. Chem. Int. Ed. **2024**, e202412983 (6 of 10)

© 2024 Wiley-VCH GmbH

rich phase at the top near the anode, which constructed a structure akin to the p-n junction from top to bottom.[20] We attributed this configuration of the donor-rich phase and acceptor-rich phase to the different surface energies of the donor and acceptor,[21] as suggested by the contact angle measurements (Figure S14 and Table S10). In addition, more obvious vertical phase segregation was found for the blends treated with SF-1 and SF-2 than for the blends without additives. The SF-2-based blends exhibited the largest component ratio of donors near the anode, which encouraged efficient charge transport due to the improved built-in potential of the devices. The above results demonstrated that a more ideal vertical phase distribution occurs after the reconstruction of the blend morphology derived from the solid additives SF-1 and SF-2, and the latter is more effective.

Because the performance of devices is highly dependent on the film morphology, further investigations on the effect of solid additives of SF-1 and SF-2 on the phase separation of the active layer was carried out by atomic force micro-

scopy (AFM). As shown in Figure 4a–c, the SF-1- and SF-2-treated blends showed successively increased root-mean-square roughness (R_q) values of 1.27 and 1.46 nm, respectively, compared with those of the additive-free blend (1.08 nm), which indicated the existence of multiscale phase domains in the additive-treated films. Then, we performed atomic force microscopy-infrared spectroscopy (AFM-IR) measurements according to the C≡N stretching vibration characteristic absorption peak of the end group characterized by infrared (IR) absorption spectra to probe the fibril structure in the additive-free or additive and additive-free/thermal annealing or additive/thermal annealing blends. In view of the unique existence of the infrared vibration signal of C≡N between PM6 and PY-DT (which only exists in PY-DT), the donor and acceptor could be identified by AFM-IR measurements. In Figure 4d–i, blue and yellow indicate the donor PM6 and acceptor PY-DT, respectively. The donor and acceptor in the additive-free thin film displayed robust aggregation (Figure 4d), and post-treatment with thermal annealing aggravated the fibril aggregation and
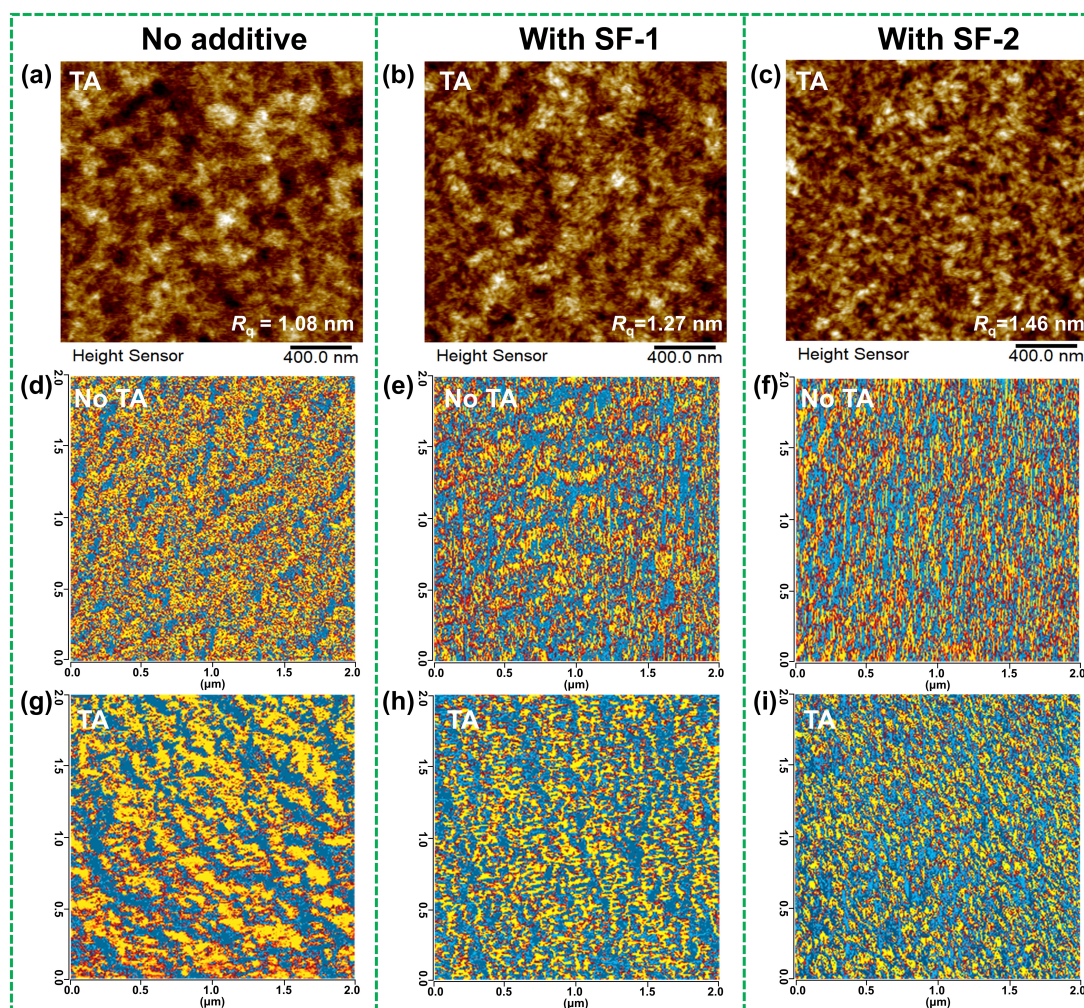

Figure 4. (a–c) AFM height images of as-cast, SF-1-treated, and SF-2-treated PM6 : PY-DT film, respectively. (d–f) AFM-IR images of PM6 : PY-DT film without and with different solid additives, respectively. (g–i) AFM-IR images of PM6 : PY-DT film without and with different solid additives after thermal annealing, respectively.

resulted in excessive phase separation, as shown in Figure 4g. In contrast, Figure 4e–f intuitively shows that the blended films exhibit more continuous phase separation with small phase-separated domains upon introduction of additives into the blends. The attenuated aggregation was ascribed to impaired self-preaggregation during film formation, stemming from the "chain-breaking"-like effect of SF-1 and SF-2 on PM6 and PY-DT.[22] Obviously, the "chain-breaking"-like effect of the solid additives SF-1 and SF-2 inhibited excessive aggregation and formed more D/A interfaces between the donor and acceptor, supporting more efficient exciton dissociation and charge transport. Interestingly, following thermal annealing, the blends initiated a "self-healing"-like process facilitated by interactions between the donor and acceptor, as well as the vacant spaces created by the evaporation of additives, leading to the formation of purer and more continuous domains of active materials. The "chain-breaking"-like and "self-healing"-like processes, influenced by SF-1 and SF-2, regulated the morphology of the active layers, forming a continuous interpenetrated network crucial for the dynamic behavior of charges.

Figure S15 and Figure S16 illustrate the 2D GIWAXS diffraction patterns and corresponding line-cut profiles of the three blended films, respectively. Both films with and without additives exhibited a predominant face-on molecular orientation. In the OOP direction, the π–π stacking peaks located at 1.62, 1.61, and 1.60 Å^{-1} correspond to CLs of 26.93, 23.56, and 25.70 Å for the as-cast, SF-1-treated, and SF-2-treated films, respectively. These results revealed that

the crystallinity of the PM6:PY-DT blend films treated with SF-1 and SF-2 decreased slightly, which is conducive to constructing multiscale phase domains and contributes to increased J_{sc} and FF. The addition of SF-1- and SF-2-shaped interpenetrated networks with large numbers of D/A interfaces provided more transport channels, resulting in higher J_{sc} and FF in APSCs processed by SF-1 and SF-2.

To understand effects of the morphological optimization on the charge dynamics induced by the solvent additives, we explored the exciton diffusion and charge generation processes by transient absorption spectroscopy (TAS). We selectively excited the acceptor component, PY-DT, using 800 nm light pulses. The 2D color plots of the TA images for the blends without and with additives are illustrated in Figure 5a–c, and the corresponding TA spectra recorded at different probe delay times are displayed in Figure 5d–f. The prompt signal at ≈890 nm was assigned to the photo-induced absorption (PIA) of the exciton of PY-DT.[23] Following the selective excitation, the hole-transfer behavior from the acceptor to the donor was monitored by the rise of the ground-state bleaching (GSB) signals of PM6 at 630 nm (Figure S17). The TA GSB decay kinetics of the PM6:PY-DT films treated with SF-1 or SF-2 at 630 nm demonstrated τ_{avg} values of 0.73 and 0.36 ps, respectively, which are shorter than those of the control blend ($\tau_{avg} = 0.94$ ps) (Table S11, the fitting parameters at 1000 nm of PM6:PY-DT blends was summarized in Table S12).[3f,23] This, surprisingly, is consistent with the morphological observations "chain-breaking"-like effect, where smaller domains are created,
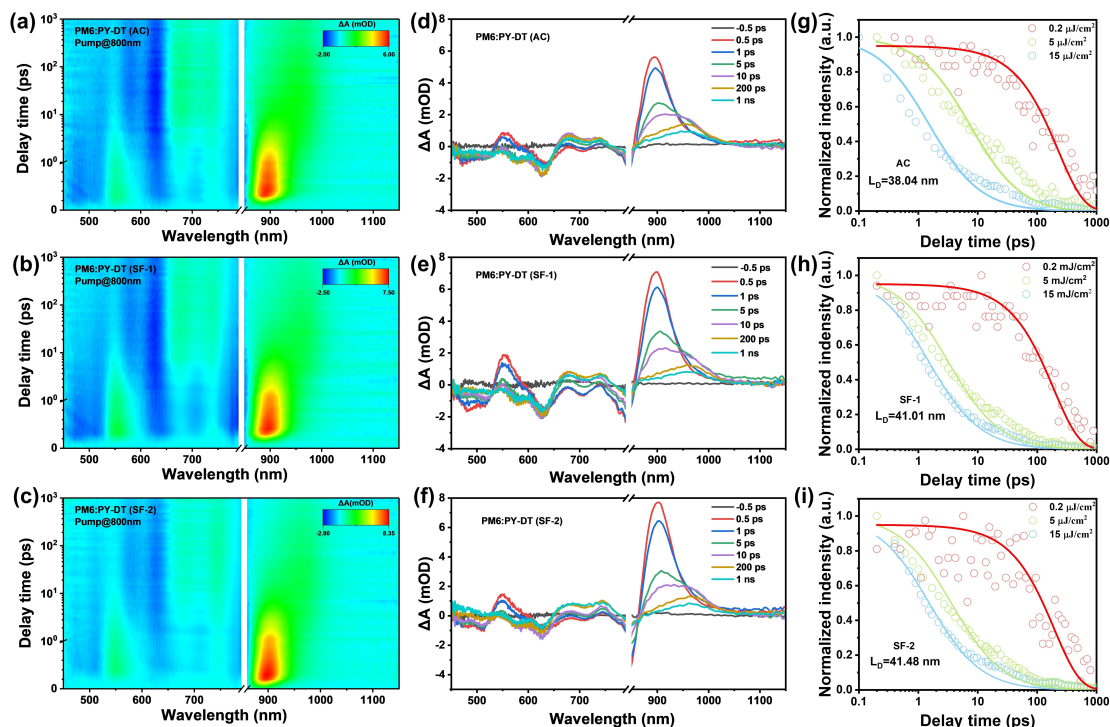

Figure 5. Transient absorption spectra of different PM6:PY-DT blends pumped with 800 nm. (a–c) 2D TAS images and (d–f) corresponding TA spectra at different probe delay times of PM6:PY-DT films processed with different conditions. (g–i) Dynamics of the singlet excitons measured with 800 nm pump excitation at different densities in PY-DT films treated without and with SF-1/SF-2 additives.

Angew. Chem. Int. Ed. **2024**, e202412983 (8 of 10)

© 2024 Wiley-VCH GmbH

favorable for exciton dissociation (detailed descriptions are provided in the Supporting Information).

Furthermore, we further investigated the L_D using the exciton-exciton annihilation (EEA) method[24] via pump-fluence-dependent TAS to explore the effect of the additives SF-1 and SF-2 on the excitonic behavior, as shown in Figure 5g–i.[25] The EEA method posits that there are two primary pathways for exciton quenching channels: radiative and non-radiative deactivation characterized by an intrinsic exciton lifetime constant ($k = 1/\tau$, where τ represents the exciton lifetime) and the bimolecular decay rate coefficient (γ) for the bimolecular EEA. We calculated the L_D according to the equation $L_D = \sqrt{D\tau}$, where D represents the exciton diffusion coefficient (the detailed calculation processes are presented in the Supporting Information, and the relevant parameters are summarized in Figure S18 and Table S13). The extracted L_D values of the SF-1- and SF-2-processed films (41.01 and 41.48 nm, respectively) were slightly greater than that of the as-casted film (38.04 nm). These data revealed that the presence of the solid additives SF-1 and SF-2 enhanced exciton diffusion, favoring efficient exciton dissociation. Overall, the addition of SF-1 or SF-2 promoted the formation of films with longer L_D and smaller domain sizes, facilitating exciton diffusion to the D/A interface and efficiently competing with exciton recombination, thereby promoting exciton dissociation and charge generation.

Conclusion

In conclusion, the PCEs of APSCs are promoted by synthesizing benzo-c-1,2,5-thiadiazole-based volatile solid additives SF-1 and SF-2, which are isomers with fluorine atoms at different substitution positions, contributing to different interactions with donors and acceptors. We investigated the effects of introducing SF-1 or SF-2 on the phase separation, film morphology, and photovoltaic properties of PM6:PY-DT PSCs. The two solid additives both exhibited the ability to reconstruct the morphology of active layer films, enabling the formation of a continuous interpenetrated network and multiscale phase domains with abundant D/A interfaces. This resulted in more efficient exciton diffusion and dissociation as well as a rapid exciton extraction and charge transport. These favorable conditions give rise to an SF-2-treated APSC with a high PCE of 18.83 % and excellent thermal stability, representing one of the best results of all-polymer organic solar cells. Our work identified an intriguing solid additive family for reconstructing film morphology and provided a method for fabricating high-performance devices. We believe that further innovation of novel polymer photovoltaic materials and device fabrication processes, such as the volatile solid additive strategy, will boost the PCEs of APSCs, allowing their application in flexible and wearable devices.

Conflict of Interest

The authors declare no conflict of interest.

Data Availability Statement

The data that support the findings of this study are available from the corresponding author upon reasonable request.

[1] a) R. Zeng, L. Zhu, M. Zhang, W. Zhong, G. Zhou, J. Zhuang, T. Hao, Z. Zhou, L. Zhou, N. Hartmann, X. Xue, H. Jing, F. Han, Y. Bai, H. Wu, Z. Tang, Y. Zou, H. Zhu, C.-C. Chen, Y. Zhang, F. Liu, *Nat. Commun.* **2023**, *14*, 4148; b) R. Sun, W. Wang, H. Yu, Z. Chen, X. Xia, H. Shen, J. Guo, M. Shi, Y. Zheng, Y. Wu, W. Yang, T. Wang, Q. Wu, Y. Yang, X. Lu, J. Xia, C. J. Brabec, H. Yan, Y. Li, J. Min, *Joule* **2021**, *5*, 1548–1565; c) Z. Genene, W. Mammo, E. Wang, M. R. Andersson, *Adv. Mater.* **2019**, *31*, e1807275; d) G. Wang, F. S. Melkonyan, A. Facchetti, T. J. Marks, *Angew. Chem. Int. Ed.* **2019**, *58*, 4129–4142; e) C. Lee, S. Lee, G.-U. Kim, W. Lee, B. J. Kim, *Chem. Rev.* **2019**, *119*, 8028–8086; f) T. Wang, M. Chen, R. Sun, J. Min, *Chem* **2023**, *9*, 1702–1767; g) T. Kim, J.-H. Kim, T. E. Kang, C. Lee, H. Kang, M. Shin, C. Wang, B. Ma, U. Jeong, T.-S. Kim, B. J. Kim, *Nat. Commun.* **2015**, *6*, 8547; h) T. Chen, X. Zheng, D. Wang, Y. Zhu, Y. Ouyang, J. Xue, M. Wang, S. Wang, W. Ma, C. Zhang, Z. Ma, S. Li, L. Zuo, H. Chen, *Adv. Mater.* **2023**, *36*, 2308061.

[2] P. Wu, Y. Duan, Y. Li, X. Xu, R. Li, L. Yu, Q. Peng, *Adv. Mater.* **2023**, *36*, 2306990.

[3] a) M. Deng, X. Xu, W. Qiu, Y. Duan, R. Li, L. Yu, Q. Peng, *Angew. Chem. Int. Ed.* **2024**, e202405243; b) J. Wang, Y. Li, C. Han, L. Chen, F. Bi, Z. Hu, C. Yang, X. Bao, J. Chu, *Energy Environ. Sci.* **2024**, *17*, 4216–4227; c) W. Xu, H. Tian, Y. Ni, Y. Xu, L. Zhang, F. Zhang, S. Wu, S. Young Jeong, T. Huang, X.

Angew. Chem. Int. Ed. **2024**, e202412983 (9 of 10)

© 2024 Wiley-VCH GmbH

Du, X. Li, Z. Ma, H. Young Woo, J. Zhang, X. Ma, J. Wang, F. Zhang, *Chem. Eng. J.* **2024**, *493*, 152558; d) Z. G. Zhang, Y. Li, *Angew. Chem. Int. Ed.* **2020**, *60*, 4422–4433; e) M. Xiao, L. Liu, Y. Meng, B. Fan, W. Su, C. Jin, L. Liao, F. Yi, C. Xu, R. Zhang, A. K. Y. Jen, W. Ma, Q. Fan, *Sci. China Chem.* **2023**, *66*, 1500–1510; f) Z. Ge, J. Qiao, Y. Li, J. Song, C. Zhang, Z. Fu, M. H. Jee, X. Hao, H. Y. Woo, Y. Sun, *Adv. Mater.* **2023**, *35*, 2301906.

[4] X.-M. Zhu, S.-N. Bao, H. Yang, H.-Y. Fan, C.-L. Fan, X.-X. Li, K.-W. Hu, H.-Y. Cao, C.-H. Cui, Y.-F. Li, *Chin. J. Polym. Sci.* **2022**, *40*, 960–967.

[5] a) L. Wang, C. Chen, Y. Fu, C. Guo, D. Li, J. Cheng, W. Sun, Z. Gan, Y. Sun, B. Zhou, C. Liu, D. Liu, W. Li, T. Wang, *Nat. Energy* **2024**, *9*, 208–218; b) D. Hu, H. Tang, C. Chen, P. Huang, Z. Shen, H. Li, H. Liu, C. E. Petoukhoff, J. P. Jurado, Y. Luo, H. Xia, P. W. K. Fong, J. Fu, L. Zhao, C. Yan, Y. Chen, P. Cheng, X. Lu, G. Li, F. Laquai, Z. Xiao, *Adv. Mater.* **2024**, *36*, 2402833.

[6] a) Y. Xu, J. Wang, T. Zhang, Z. Chen, K. Xian, Z. Li, Y.-H. Luo, L. Ye, X. Hao, H. Yao, J. Hou, *Energy Environ. Sci.* **2023**, *16*, 5863–5870; b) Q. Chen, Z. Bian, Y. Yang, X. Cui, C. Jeffreys, X. Xu, W. Li, Y. Liu, M. Henney, Z. Bo, *Angew. Chem. Int. Ed.* **2024**, e202405949.

[7] J. K. Lee, W. L. Ma, C. J. Brabec, J. Yuen, J. J S. Moon, J. Y. Kim, K. Lee, G. C. Bazan, A. J. Heeger, *J. Am. Chem. Soc.* **2008**, *130*, 3619.

[8] C. V. Hoven, X. D. Dang, R. C. Coffin, J. Peet, T. Q. Nguyen, G. C. Bazan, *Adv. Mater.* **2010**, *22*, E63–E66.

[9] a) G. Cai, Z. Chen, X. Xia, Y. Li, J. Wang, H. Liu, P. Sun, C. Li, R. Ma, Y. Zhou, W. Chi, J. Zhang, H. Zhu, J. Xu, H. Yan, X. Zhan, X. Lu, *Adv. Sci.* **2022**, *9*, 2200578; b) B. J. Tremolet de Villers, K. A. O'Hara, D. P. Ostrowski, P. H. Biddle, S. E. Shaheen, M. L. Chabinyc, D. C. Olson, N. Kopidakis, *Chem. Mater.* **2016**, *28*, 876–884; c) C. McDowell, M. Abdelsamie, M. F. Toney, G. C. Bazan, *Adv. Mater.* **2018**, *30*, 1707114.

[10] a) R. Yu, H. Yao, L. Hong, Y. Qin, J. Zhu, Y. Cui, S. Li, J. Hou, *Nat. Commun.* **2018**, *9*, 4645; b) K. Hu, C. Zhu, K. Ding, S. Qin, W. Lai, J. Du, J. Zhang, Z. Wei, X. Li, Z. Zhang, L. Meng, H. Ade, Y. Li, *Energy Environ. Sci.* **2022**, *15*, 4157–4166; c) Z. Jia, J. Pan, X. Chen, Y. Li, T. Liu, H. Zhu, J. Yao, B. Yan, Y. Yang, *Energy Environ. Sci.* **2024**, *17*, 3908–3916.

[11] J. Y. Lu Chen, R. Ma, L. Ding, T. A. Dela Peña, H. Liu, J. Chen, C. Zhang, C. Zhao, W. Lu, Q. Wei, B. Zhao, H. Hu, J. Wu, Z. Ma, X. Lu, M. Li, G. Zhang, G. Li, H. Yan, *Adv. Mater.* **2023**, *35*, 2301231.

[12] X. Cao, J. Guo, Z. Li, X. Bi, H. Liang, Z. Xiao, Y. Guo, X. Jia, Z. Xu, K. Ma, Z. Yao, B. Kan, X. Wan, C. Li, Y. Chen, *ACS Energy Lett.* **2023**, *8*, 3494–3503.

[13] J. Song, Y. Li, Y. Cai, R. Zhang, S. Wang, J. Xin, L. Han, D. Wei, W. Ma, F. Gao, Y. Sun, *Matter* **2022**, *5*, 4047–4059.

[14] W. Feng, T. Chen, Y. Li, T. Duan, X. Jiang, C. Zhong, Y. Zhang, J. Yu, G. Lu, X. Wan, B. Kan, Y. Chen, *Angew. Chem. Int. Ed.* **2024**, *63*, e202316698.

[15] a) L. Tu, H. Wang, W. Duan, R. Ma, T. Jia, T. A. Dela Peña, Y. Luo, J. Wu, M. Li, X. Xia, S. Wu, K. Chen, Y. Wu, Y. Huang, K. Yang, G. Li, Y. Shi, *Energy Environ. Sci.* **2024**, 3365–3374; b) D. Zhang, Y. Li, M. Li, W. Zhong, T. Heumüller, N. Li, L. Ying, C. J. Brabec, F. Huang, *Adv. Funct. Mater.* **2022**, *32*, 2205338; c) Y. Wang, Z. Liang, X. Liang, X. Wen, Z. Cai, Z. Shao, J. Zhang, Y. Ran, L. Yan, G. Lu, F. Huang, L. Hou, *Adv. Energy Mater.* **2023**, *13*, 2300524; d) T. Chen, Y. Bai, X. Ji, W. Feng, T. Duan, X. Jiang, Y.-q.-q. Yi, J. Yu, G. Lu, X. Wan, B. Kan, Y. Chen, *Nano Energy* **2024**, *125*, 109604; e) S. Bao, H. Yang, H. Fan, J. Zhang, Z. Wei, C. Cui, Y. Li, *Adv. Mater.* **2021**, *33*, 2105301.

[16] Q. Nie, A. Tang, Q. Guo, E. Zhou, *Nano Energy* **2021**, *87*, 106174.

[17] J. Yuan, Y. Zhang, L. Zhou, G. Zhang, H.-L. Yip, T.-K. Lau, X. Lu, C. Zhu, H. Peng, P. A. Johnson, M. Leclerc, Y. Cao, J. Ulanski, Y. Li, Y. Zou, *Joule* **2019**, *3*, 1140–1151.

[18] a) M. Zhang, X. Guo, W. Ma, H. Ade, J. Hou, *Adv. Mater.* **2015**, *27*, 4655–4660; b) Y. Li, J. Song, Y. Dong, H. Jin, J. Xin, S. Wang, Y. Cai, L. Jiang, W. Ma, Z. Tang, Y. Sun, *Adv. Mater.* **2022**, *34*, 2110155.

[19] B. Fan, W. Zhong, W. Gao, H. Fu, F. R. Lin, R. W. Y. Wong, M. Liu, C. Zhu, C. Wang, H. L. Yip, F. Liu, A. K. Y. Jen, *Adv. Mater.* **2023**, *35*, 2302861.

[20] Z. Ge, J. Qiao, J. Song, X. Li, J. Fu, Z. Fu, J. Gao, X. Tang, L. Jiang, Z. Tang, G. Lu, X. Hao, Y. Sun, *Adv. Energy Mater.* **2024**, *14*, 2400203.

[21] H. Hu, S. Liu, J. Xu, R. Ma, Z. Peng, T. A. D. Peña, Y. Cui, W. Liang, X. Zhou, S. Luo, H. Yu, M. Li, J. Wu, S. Chen, G. Li, Y. Chen, *Angew. Chem. Int. Ed.* **2024**, *63*, e202400086.

[22] a) M. R. Buche, M. N. Silberstein, *J. Mech. Phys. Solids* **2021**, *156*, 104593; b) Y. Lin, T. B. Kouznetsova, C.-C. Chang, S. L. Craig, *Nat. Commun.* **2020**, *11*, 4987; c) Y. Tian, M. V. Kuzimenkova, M. Xie, M. Meyer, P.-O. Larsson, I. G. Scheblykin, *NPG Asia Mater.* **2014**, *6*, e134–e134.

[23] Z. Fu, J. W. Qiao, F. Z. Cui, W. Q. Zhang, L. H. Wang, P. Lu, H. Yin, X. Y. Du, W. Qin, X. T. Hao, *Adv. Mater.* **2024**, *36*, 2313532.

[24] P. Bi, S. Zhang, Z. Chen, Y. Xu, Y. Cui, T. Zhang, J. Ren, J. Qin, L. Hong, X. Hao, J. Hou, *Joule* **2021**, *5*, 2408–2419.

[25] a) S. Chandrabose, K. Chen, A. J. Barker, J. J. Sutton, S. K. K. Prasad, J. Zhu, J. Zhou, K. C. Gordon, Z. Xie, X. Zhan, J. M. Hodgkiss, *J. Am. Chem. Soc.* **2019**, *141*, 6922–6929; b) J. Wang, Y. Xie, K. Chen, H. Wu, J. M. Hodgkiss, X. Zhan, *Nat. Rev. Phys.* **2024**, *6*, 365–381.
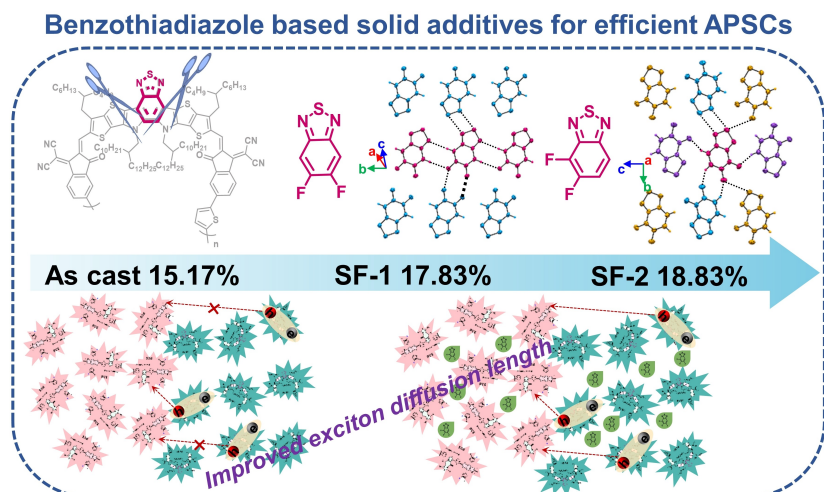
Research Article

Solar Cells

T. Chen, Y. Zhong, T. Duan,* X. Tang,
W. Zhao, J. Wang, G. Lu, G. Long,
J. Zhang,* K. Han, X. Wan, B. Kan,*
Y. Chen ————— e202412983

Asymmetrified Benzothiadiazole-Solid Additives Enable All-Polymer Solar Cells with Efficiency Over 19%

Benzothiadiazole based solid additives for efficient APSCs

As cast 15.17%   SF-1 17.83%   SF-2 18.83%

Two electron-deficient isomers, 4,5-difluorobenzo-*c*-1,2,5-thiadiazole (SF-1) and 5,6-difluorobenzo-*c*-1,2,5-thiadiazole (SF-2), were designed as solid additives to optimize the properties of PM6 : PY-DT blend. Compared to the as-cast device, SF-1- and SF-2-treated devices displayed regulated fibrillar donor-acceptor network, improved exciton diffusion length, and thus enhanced power conversion efficiencies approaching 19%, which is one of rare solid additives for high-performance all-polymer organic solar cells.